Journal of Materials Chemistry B

PAPER

View Article Online
View Journal | View Issue

Cite this: J. Mater. Chem. B, 2018, 6, 1508

Oral administration of highly bright Cr^{3+} doped $ZnGa_2O_4$ nanocrystals for *in vivo* targeted imaging of orthotopic breast cancer†

Hanghang Liu,[a] Feng Ren,[a] Hao Zhang,[a] Yaobao Han,[a] Huizhu Qin,[b] Jianfeng Zeng,[a] Yong Wang,[a] Qiao Sun,[a] Zhen Li*[a] and Mingyuan Gao[a]

Received 6th December 2017,
Accepted 5th February 2018

DOI: 10.1039/c7tb03148c

rsc.li/materials-b

Near-infrared (NIR) long lasting persistent luminescence nanoparticles (PLNPs) have attracted considerable attention in the area of *in vivo* bioimaging, due to their background-free luminescence characteristics and deep tissue penetration. However, the low fluorescence quantum yield and short afterglow of the currently available PLNPs limit their applications. Here, water-soluble Cr^{3+}-doped $ZnGa_2O_4$ PLNPs with the highest quantum yield (η = 20%) ever reported, bright NIR emission, and excellent colloidal stability were successfully prepared by a one-step hydrothermal method. The afterglow of the resultant nanocrystals lasted for more than 5 days and could be repeatedly reactivated by the light (λ = 657 nm) of a portable light emitting diode lamp after decay. These nanocrystals were functionalized with α,ω-dicarboxyl-terminated poly(ethylene glycol) and poly(acrylic acid) to improve their stability and biocompatibility, so that they could be conjugated with a c(RGDyK) peptide and labeled with ^{99m}Tc for targeted imaging of orthotopic breast cancer by afterglow luminescence imaging and single-photon emission computed tomography imaging. Our NIR-PLNP probes can effectively avoid tissue auto-fluorescence and the light scattering caused by continuous excitation during the diagnosis of cancer.

Introduction

Various kinds of molecular imaging, such as optical imaging,[1] ultrasound imaging,[2,3] magnetic resonance imaging (MRI),[4] and nuclear imaging,[5] have played significant roles in the diagnosis and treatment of cancer, among which, optical imaging (*e.g.*, photoluminescence) has received considerable attention because of its merits of high sensitivity, low cost, good compatibility and portability, and avoidance of harmful radiation.[6] It can easily be integrated with other imaging modalities and used for diagnosis and/or imaging guided therapy. Many types of luminescent probes,[7] such as organic dyes,[8,9] fluorescent proteins,[10] semiconductor quantum dots,[11–13] metal nanoclusters,[14,15] and up-conversion nanocrystals,[16–18] have been developed. The *in vivo* fluorescence imaging based on the above probes, however, has issues of limited resolution and/or depth penetration due to the strong tissue auto-fluorescence and light scattering arising from their *in situ* continuous excitation.[19,20] An alternative probe is near-infrared (NIR) long-lasting persistent luminescence nanoparticles (PLNPs), which work like rechargeable batteries and with persistent photoluminescence that can last for several hours even many days after they are "photo-charged" for a few minutes.[21–26] These *ex situ* excited PLNPs have excellent chemical and thermal stability,[27] minimal tissue auto-fluorescence and background interference, and less toxicity induced by light after they are delivered into the body.[28,29] There are a few types of PLNPs reported for *in vivo* animal imaging and therapy, of which Cr^{3+} doped zinc gallate (*i.e.*, ZGC) has become one of the most attractive phosphors because it emits a NIR persistent luminescence with a tunable afterglow time.[21,30]

From the perspective of applications, there are increasing demands for long afterglow from PLNPs for long-term bio-imaging.[31] The existing ZGC-based PLNPs have an afterglow varying from several minutes to a few days, strongly depending on the preparation methods. For example, 10 nm ZGC nanoparticles prepared *via* a biphasic hydrothermal route emitted NIR persistent luminescence for more than 40 min after the excitation was switched off.[23] Furthmore, a two-hour afterglow was observed for larger ZGC nanoparticles with a size of 20–60 nm, which were synthesized by the hydrothermal method and then sintered in air at low temperature.[21] Longer afterglow (>4 h) was also achieved in ultra-small ZGC nanoparticles

[a] Center for Molecular Imaging and Nuclear Medicine, State Key Laboratory of Radiation Medicine and Protection, School for Radiological and Interdisciplinary Sciences (RAD-X), Soochow University, Collaborative Innovation Center of Radiation Medicine of Jiangsu Higher Education Institutions, Suzhou 215123, China. E-mail: zhenli@suda.edu.cn

[b] Medical School of Nantong University, Clinical Medicine, Nantong 226019, China

† Electronic supplementary information (ESI) available. See DOI: 10.1039/c7tb03148c

(6 nm) fabricated by a non-aqueous sol–gel method with the assistance of microwave irradiation.[32]

The afterglow time of ZGC-based PLNPs can be prolonged by engineering their compositions.[33] For example, co-doping of Cr^{3+} and Pr^{3+} ions into $Zn_{2.94}Ga_{1.96}Ge_2O_{10}$ through a sol–gel method led to a very long afterglow (>15 days) of the resultant nanopowders.[29] By using a solid state reaction at high temperature, a series of Cr^{3+}-doped zinc gallate bulk NIR persistent phosphors with a long afterglow of more than 360 h were obtained.[34] The engineered Zn–Ga–Sn–O solids also exhibited long persistent luminescence over 300 h.[35,36] These high-quality bulk ZGC could be milled into nanopowders and then modified for bioapplications, although the resultant nanoparticles had issues of reduced afterglow, large particle size, poor homogeneity, poor water-solubility, and colloidal instability, which are unfavorable for *in vivo* applications.

Besides the long afterglow luminescence, the ideal PLNPs for bioapplications should also exhibit excellent water-solubility and biocompatibility after surface functionalization[37] and therapeutic functions. They should be able to be repeatedly excited *in situ* for imaging and therapy by the light from a portable light emitting diode (LED) or NIR laser.[21,38–41] For example, the use of 808 nm NIR light for excitation could overcome the issues of deep tissue-penetration, overheating, and strong irradiation energy,[42] which is beneficial for the photodynamic therapy (PDT) of tumors. For the fabrication of PDT platforms, ZGC PLNPs were either conjugated or made to adsorb photosensitizers, which were directly excited by the emission from the ZGC nanoparticles. Recently, there has been a report on ZGC nanoparticle enhanced cancer cell death.[43] An injectable persistent luminescence implant as a built-in excitation source for efficient repeatable photodynamic therapy was demonstrated.[44] In addition, ZGC nanocrystals were also coated with mesoporous SiO_2 shells for drug delivery,[45,46] and for tracking the metabolism of drugs.[47]

The above examples clearly illustrate the great potential of ZGC-based PLNPs in bioimaging and tumor therapy. The most currently available ZGC nanoparticles, however, have one or more of the following disadvantages: low fluorescence quantum efficiency, short decay time, large particle size with a broad size distribution, poor water solubility, or less biocompatibility. These factors significantly influence their performance when they are used for *in vivo* imaging and therapy. From an imaging perspective, most ZGC nanoprobes have only been used for luminescence imaging, which has limitations in sensitivity because of a weak luminescence intensity and low quantum yield. An alternative is the functionalization of ZGC nanocrystals with other imaging modalities, such as MRI,[4,48–51] and nuclear imaging.[52] In terms of therapy (*e.g.*, PDT), the emission intensity and yield also directly determine the efficacy of the therapy. The highest absolute fluorescent quantum yield of the currently available ZGC nanocrystals is around 10%,[23,39] however. In this context, the preparation of water-soluble and biocompatible monodispersed ZGC nanoparticles with a high quantum yield, long afterglow, and multifunctions is highly significant.

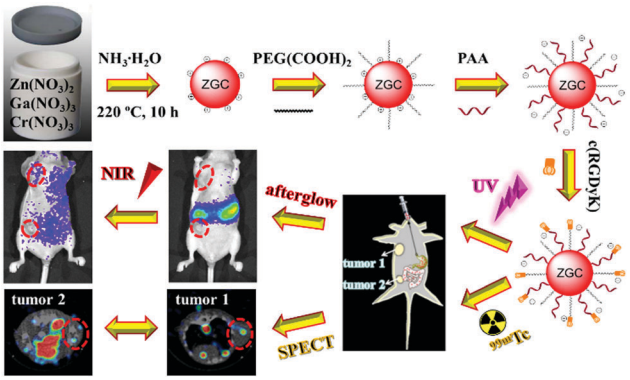

Scheme 1 Schematic illustration of the synthesis of multifunctional ZGC nanocrystals, and *in vivo* afterglow imaging and SPECT/CT imaging of a mouse after intra-gastric administration of the nanocrystals.

In this article, size-tunable highly bright, water-soluble Cr^{3+}-doped $ZnGa_2O_4$ (ZGC) nanoparticles are prepared by the one-step hydrothermal method, and then functionalized with poly(ethylene glycol) (PEG) and poly(acrylic acid) (PAA) for conjugation with a c(RGDyK) peptide and labeling with radioactive nuclide ^{99m}Tc (Scheme 1). The functional ZGC nanoparticles exhibited the highest absolute photoluminescence quantum yield (η = 20%) ever reported, and a long afterglow (up to 5 days), making them suitable for background-free targeted imaging of an orthotopic murine model of breast cancer by afterglow luminescence imaging and single-photon emission computed tomography (SPECT)/computed tomography (CT) imaging (Scheme 1).

Results and discussion

As illustrated in Scheme 1, the ZGC nanocrystals were prepared using a hydrothermal method. Compared with the conventional hydrothermal approach, ammonium hydroxide solution rather than NaOH was selected to control the pH of the mixed solution, as the excessive ammonium can easily evaporate.[38] The size of the ZGC nanocrystals can be tuned by changing the reaction parameters as shown in Table 1.

Fig. 1(a–d) show the transmission electron microscopy (TEM) images of the purified ZGC nanoparticles, which have narrow size distributions (Fig. S1 in the ESI†) and average sizes of 8.7, 14.2, 20.6, and 32.4 nm, respectively. These nanoparticle samples are referred to as ZGC-8, ZGC-14, ZGC-20, and ZGC-32, respectively. The crystal structures of the as-synthesized ZGC nanoparticles were examined by powder X-ray diffraction (XRD) (Fig. 1e). The narrow and sharp diffraction peaks suggest that the ZGC nanoparticles were well crystallized under the hydrothermal conditions. The good crystallinity is also demonstrated by a typical high resolution TEM (HRTEM) image (Fig. S2a, ESI†), the lattice planes of which have a spacing of 0.208 nm, corresponding to the (400) planes of spinel $ZnGa_2O_4$. In addition, all the diffraction peaks match well with those of cubic spinel $ZnGa_2O_4$ (JCPDS No. 38-1240) as shown in Fig. 1e and Fig. S2b (ESI†), indicating the high purity of the resultant ZGC

Table 1 Synthesis of different sized ZGC NCs

NCs	$Zn(NO_3)_3{\cdot}6H_2O$ (mmol)	$Ga(NO_3)_3{\cdot}xH_2O$ (mmol)	$Cr(NO_3)_3{\cdot}9H_2O$ (mmol)	Particle size (TEM, nm)	Quantum yield (%)
ZGC-8	1.2	2	0.004	8.7 ± 0.9	12.04
ZGC-14	3.6	6	0.012	14.2 ± 1.7	19.60
ZGC-20	0.8	1.33	0.0027	20.6 ± 1.9	6.45
ZGC-32	0.4	0.67	0.00135	32.4 ± 4.4	9.36

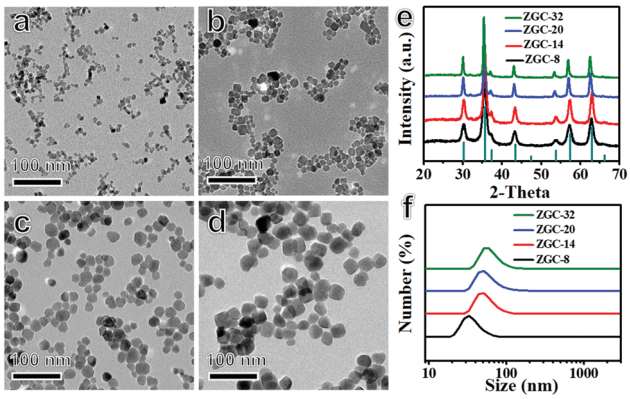

Fig. 1 (a–d) TEM images of ZGC-8, ZGC-14, ZGC-20, and ZGC-32, respectively, and the corresponding (e) XRD patterns, and (f) hydrodynamic sizes.

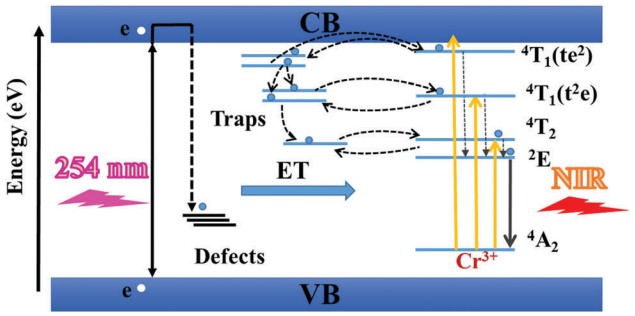

Fig. 2 Schematic description of the persistent luminescence mechanism. The energy transfer was referred to as ET.

nanocrystals and successful removal of impurities with a diluted HCl solution. The high purity of the resultant nanoparticles can be also proved by the atomic ratio of Zn : Ga : O, which was determined using energy dispersive X-ray spectroscopy (EDX) to be 1 : 2 : 4 (Fig. S3, ESI†), which is consistent with the theoretical ratio.

The purified ZGC nanoparticles can be well dispersed in water because of their positively charged surface, *e.g.*, the zeta potential of ZGC-14 is (+38.4 ± 1.5) mV. Their hydrodynamic sizes (Fig. 1f) were measured to be 32.7 nm, 43.8 nm, 50.7 nm, and 58.8 nm, respectively, using a dynamic laser scattering (DLS) method. The ultraviolet-visible (UV-vis) absorbance of different-sized ZGC nanocrystal solutions with the same concentration of nanoparticles (0.5 mg mL^{-1}) is compared in Fig. S4a (ESI†), where no obvious absorption peak is observed. They exhibit an intense fluorescence in the range of 600–800 nm with two typical emissions located at 696 nm and 712 nm [Fig. S4(b and c), ESI†]. The former peak is attributed to the $^2E \rightarrow 4A^2$ transition from the distorted Cr^{3+} ions in gallate related to an antisite defect,[29,48,53] which is due to the fact that the phonon energy of the Cr^{3+} dopant matches well with that of the gallate-containing host.[54,55] The latter peak is ascribed to the anti-Stokes phonon side bands (PSB).[21,29] The surface zeta potential in Fig. S4d (ESI†) shows the negligible difference between these different-sized nanocrystals.

It should be noted that the photoluminescence peaks of these ZGC nanocrystals are size-independent (Fig. S4b, ESI†), which could be due to their unique luminescence mechanism. As shown in Fig. 2, upon UV light (254 nm) excitation, the electrons are generated and transited from the valence band (VB) to the conduction band (CB) of the $ZnGa_2O_4$ nanoparticles. Parts of the excited electrons are captured by their native defects of $ZnGa_2O_4$. Then the energy is transferred from the $ZnGa_2O_4$ host to the Cr^{3+} ions by nonradiative energy transfer.[29] The energy transfer (ET) excites the electrons of the Cr^{3+} ions transiting from the ground state to the excited state and thus induces the persistent luminescence after UV light is turned off. The excited state electrons of the Cr^{3+} ions can be captured by traps with different depths. Electrons in the shallow traps are partially transferred to deep traps through nonradiative relaxation. Meanwhile, a slow tunneling process accompanied between the electrons in the deep traps and the nearby ionized Cr^{3+} ions results in the long term persistant luminescence.[34,39]

The absolute fluorescence quantum yields (η) of different-sized ZGC nanocrystals were respectively measured to be 12.0%, 19.6%, 6.5%, and 9.4% (Table 1), by using the De Mello method based on an integrating sphere incorporated into a spectrofluorimeter. The fluorescence quantum yield can be further improved to 27% by replacing ammonia with sodium bicarbonate. There are many factors influencing the quantum yield of ZGC nanoparticles, such as crystallinity, trap type, trap number, trap depth, and surface defects, which are strongly dependent on the preparation approach and reaction parameters.[56] The high fluorescence quantum yield could be attributed to the hydrothermal conditions and high reactant concentrations. The hydrothermal method could provide a high temperature and pressure to generate highly crystalline nanoparticles.[30] High reactant concentrations could lead to more traps and less surface defects, and result in a high fluorescence quantum yield. The results demonstrate the importance of controlling reaction conditions such as precursor concentration and base solution, and that small modifications could make a huge difference.

ZGC-14 was selected for further characterization and modification. Fig. 3a shows the excitation and emission spectra of a ZGC-14 solution with a concentration of 0.5 mg mL^{-1}.

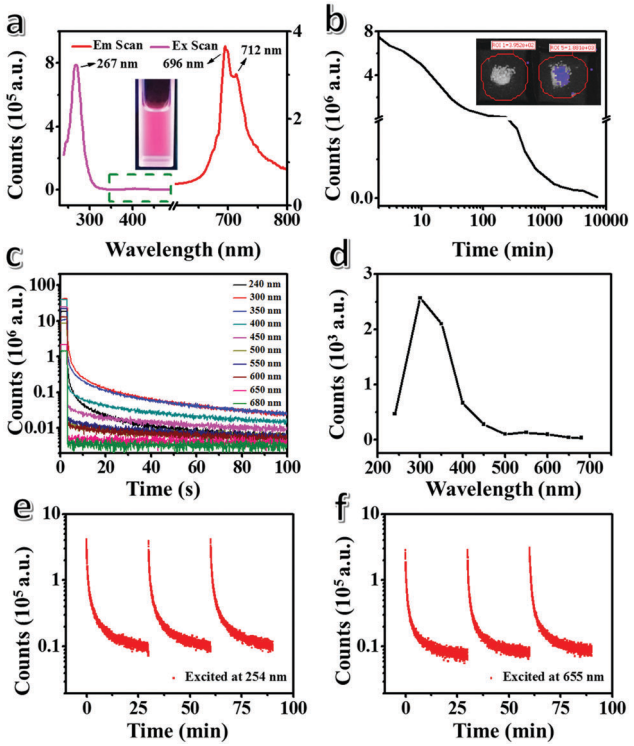

Fig. 3 (a) Emission and excitation spectra of the ZGC-14 nanocrystal solution with a concentration of 0.5 mg mL^{-1}; (b) afterglow decay curve of ZGC nanopowder after excitation with 254 nm UV light for 10 min and recording on a CCD camera, the inset shows the luminescence of the ZGC powder before excitation (left) and after decay for 5 days (right); (c) afterglow decay curves of ZGC-14 nanopowder measured with different excitation wavelengths (the emission is set at 696 nm) and (d) plot of corresponding afterglow intensities of the decay curves recorded at the 10th second after switching off the xenon lamp as a function of excitation wavelength; (e and f) afterglow decay curves of ZGC nanocrystals repeatedly reactivated with 254 nm and 657 nm light, respectively.

The strongest excitation peak at 267 nm is from the charge transfer band of Cr^{3+} between $^4A_2$ (^4F) → $^4T1$ (^4P),[47] which mainly contributed to the NIR emission at 696 nm. In addition to the main peak at 267 nm, there are two relatively weak peaks at 430 nm and 570 nm (Fig. S5a, ESI†), which come from the charge transfer of the $^4A_2$ (^4F)–$^4T_1$ (^4F) and $^4A_2$ (^4F)–$^4T_2$ (^4F) transitions of Cr^{3+} respectively.[21,34,57] To further confirm these two weak peaks, the excitation spectrum of the ZGC-14 powder was also collected (Fig. S5b, ESI†), which clearly shows the three characteristic absorbance peaks in the range of 240–680 nm. Furthermore, the emission spectrum of ZGC-14 excited at 657 nm in Fig. S5c (ESI†) shows the feasibility of excitation by a LED lamp with a wavelength of 657 nm.

An important feature of PLNPs is their ultra-long afterglow, and the long-term afterglow decay of ZGC-14 nanocrystals (NCs) was monitored through a charge coupled device (CCD) camera after being irradiated with 254 nm UV light for 10 min (Fig. 3b). The decay curve reveals that the afterglow decayed very fast in the initial 100 min, and then slowly decayed and lasted for about 5 days. Their emission spectra obtained at different times after the UV excitation was turned off (Fig. S5d, ESI†) also demonstrate the existence of long afterglow of the ZGC nanoparticles. To evaluate the effectiveness of different excitation wavelengths of afterglow luminescence, different decay curves of afterglow were measured under different excitation wavelengths in a range of 240–680 nm after the excitation light was turned off (Fig. 3c). The corresponding intensities of afterglow at 696 nm recorded at the 10th second were plotted as a function of the excitation wavelength and shown in Fig. 3d. These results shown in Fig. 3d and Fig S5b (ESI†) indicate that the ZGC-14 nanocrystals can be effectively excited by light between 240 nm and 400 nm, but less effectively by the light with a wavelength of 400 nm to 680 nm. To test their photostability and the feasibility of re-activation, the ZGC-14 nanocrystals were re-excited with 254 nm UV light and 657 nm LED light (for the spectrum of the LED light, see Fig. S5e, ESI†), respectively, after their afterglow had decayed for 30 min [Fig. 3(e and f)]. The luminescence intensities for UV and visible excitations are 4.09×10^5 and 2.84×10^5 a.u., respectively. The similar luminescence intensity and decay profile of the afterglow after each excitation with UV and red light demonstrate their excellent photostability. The re-excitation of ZGC nanocrystals with 657 nm light ensures the regeneration of luminescence after the initial decay during the long term *in vivo* imaging.

For the *in vivo* imaging, surface functionalization of the ZGC nanocrystals was conducted to achieve good colloidal stability. Because of the intensely positive charges on the surface of the ZGC nanocrystals, the α,ω-dicarboxyl-terminated PEG (M_W = 2000) and polyacrylic acid (PAA) (M_W = 3000) were attached on the surfaces of the ZGC-14 nanocrystals *via* electrostatic interactions (Scheme 1).[38] Fig. S6a (ESI†) clearly shows that the ZGC suspension became relatively transparent after modification with PEG and PAA. The Fourier transform infrared (FTIR) spectra of pristine ZGC, ZGC@PEG, and ZGC@PEG@PAA (Fig. 4a) further confirm the successful modification of nanocrystals and the presence of –COOH groups on their surface. Specifically, in the

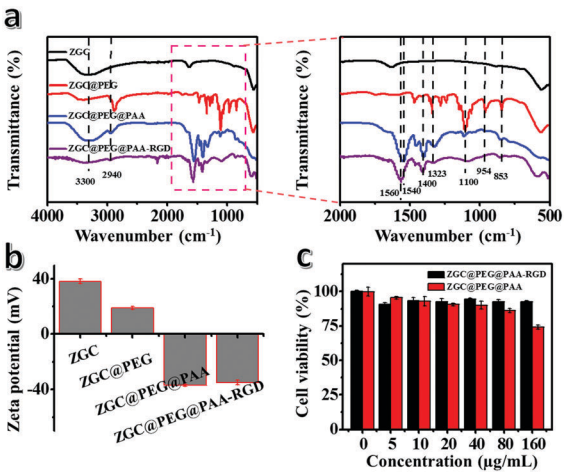

Fig. 4 (a and b) FTIR spectra and zeta potentials of pristine ZGC, ZGC@PEG, ZGC@PEG@PAA, and ZGC@PEG@PAA-arginylglycylaspartic acid (RGD), respectively; (c) *in vitro* relative cell viabilities of 4T1 cells after incubation with different concentrations of ZGC@PEG@PAA and ZGC@PEG@PAA-RGD NCs for 24 h.

spectrum of ZGC@PEG@PAA, the peaks at 3300 cm^{-1} (O–H, stretching vibration), 2940 cm^{-1} (–CH_2–, symmetrical stretching vibration), 1540 cm^{-1} (–CH_2–, bending vibration), 1323 cm^{-1} (symmetric deformation vibration), 1100 cm^{-1} (–C–O–C–, symmetrical stretching vibration), 954 cm^{-1} (–C–O–C–, in-plane deformation vibration), and 853 cm^{-1} (–CH_2CH_2O–, in-plane deformation vibration) were clearly observed. The successful modification is further demonstrated by the gradual variation of their surface charges from positive to negative (Fig. 4b), *i.e.*, the zeta potential changed from (+38.3 ± 1.51) mV for pristine ZGC, to (+19.0 ± 1.12) mV for ZGC@PEG, and (−37.1 ± 0.81) mV for ZGC@PEG@PAA. The contents of PEG and PAA that were coated on the surfaces of the ZGC nanocrystals were estimated *via* thermogravimetric analysis (TGA) (Fig. S6b, ESI†) to be 60% and 10%, respectively.

It should be noted that the surface modification did not weaken the fluorescence of the ZGC nanocrystals, as shown in Fig. S6c (ESI†). The modified ZGC nanocrystals (*i.e.*, ZGC@PEG@PAA) can be well dispersed in different media, such as H_2O, phosphate buffered saline (PBS), Roswell Park Memorial Institute (RPMI) medium, 10% fetal bovine serum (FBS), and 0.9% NaCl. The different solutions show a similar mean hydrodynamic size, as determined by dynamic light scattering (DLS) and shown in Fig. S6(d and e) (ESI†), and there is no obvious difference after 15 days of storage. The results demonstrate the excellent colloidal stability after surface modification.

The above modified nanocrystals provide functional groups to conjugate with c(RGDyK) for tumor-targeting imaging. The chemical structure of c(RGDyK) is shown in Fig. S7 (ESI†), and c(RGDyK) was conjugated with the ZGC nanocrystals through the reaction of its amine group with the carboxyl group in the PAA and HOOC–PEG–COOH under the catalysis of EDC and NHS. The FTIR spectra of the conjugates (Fig. 4a) show the typical N–H bending vibration of amide II bound with a c(RGDyK) peptide at 1560 cm^{-1} in comparison with that of a c(RGDyK) peptide, and the characteristic peaks of PEG and PAA (Fig. S7a, ESI†), demonstrating the successful conjugation of the c(RGDyK) peptide on the surfaces of the nanocrystals. The zeta potential changed slightly from −37.1 mV to −34.1 mV, and no obvious increase in hydrodynamic size was observed after the conjugation with the c(RGDyK) peptide (Fig. S7b, ESI†).

It is well known that RGD-based peptides have excellent biocompatibility, and the conjugation of RGD with ZGC@PEG@PAA not only improved the targeting efficiency but also improved the biocompatibility of the nanocrystals.[58] The potential cytotoxicity of ZGC@PEG@PAA and ZGC@PEG@PAA-RGD towards 4T1 cells was assessed through a standard methyl thiazolyl tetrazolium (MTT) assay. As shown in Fig. 4c, the results clearly illustrate the improvement of the biocompatibility of the nanocrystals after conjugation with the peptide. The cell viability remained above 90% when the nanocrystal concentration was increased from 0 to 160 μg mL^{-1}. In contrast, the cell viability gradually decreased from 100% to 75% without RGD modification as the concentration of ZGC@PEG@PAA increased to 160 μg mL^{-1}.

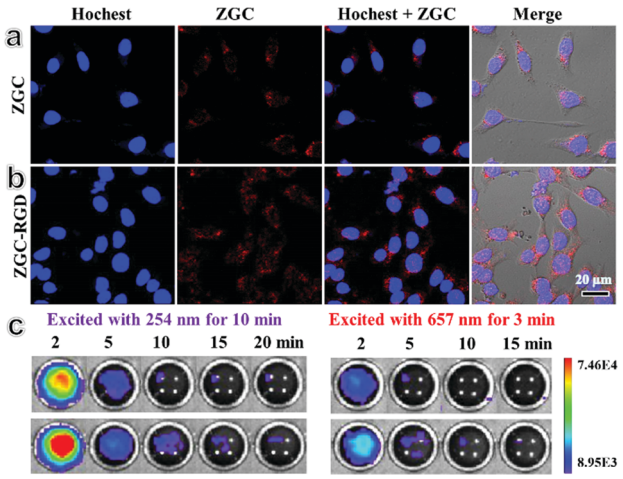

Fig. 5 Confocal fluorescence microscopy images of 4T1 cells treated with (a) ZGC@PEG@PAA, and (b) ZGC@PEG@PAA-RGD. Nuclei were stained with Hoechst 33342 in blue, and the ZGC fluorescence in the cells is red. (c) Luminescent images of ZGC@PEG@PAA (top) and ZGC@PEG@PAA-RGD (bottom) in 4T1 cells after excitation with 254 nm UV light and 657 nm LED light, respectively.

The endocytosis of RGD-modified and un-modified nanocrystals was investigated using a confocal microscope and is compared in Fig. 5(a and b). The red color is from the emission of ZGC nanocrystals excited with a 405 nm laser, and the blue color is from the nuclei of the cancer cells (*i.e.* 4T1 cells) that were stained with Hoechst 33342. The results demonstrate that the RGD-modified nanocrystals were more efficiently taken up by the 4T1 cells than the un-modified nanocrystals, due to the specific interactions of the RGD peptide with the integrin on the surfaces of the cancer cells. To further prove the endocytosis of the ZGC nanocrystals, all the cells were collected after being cultured with nanocrystals and irradiated with 254 nm UV light for 10 min, and the afterglow luminescence was recorded with a CCD camera (Fig. 5c). Although the UV light could kill the cells, it will not influence the ZGC contents in the cells which were collected and irradiated after being cultured with ZGC nanocrystals. The cells can also be re-excited with 657 nm light for 3 min using a LED lamp. The luminescence in both cases lasted for more than 10 min after excitation. The cells labeled with ZGC@PEG@PAA-RGD nanocrystals clearly exhibited a stronger afterglow under both excitation conditions, compared with those labeled with ZGC@PEG@PAA nanocrystals. This is attributed to the targeting ability of the RGD peptide. The specificity of RGD towards cancer cells was also tested by labeling the U87 cells with the ZGC@PEG@PAA-RGD and ZGC@PEG@PAA nanocrystals, respectively. The results are compared with the 4T1 cells and shown in Fig. S8 (ESI†), demonstrating the negligible difference between these two kinds of cancer cells. To further demonstrate the specificity of RGD, healthy cells (*i.e.*, NIH3T3 cells) were also labeled with the ZGC@PEG@PAA-RGD and ZGC@PEG@PAA nanocrystals (Fig. S9, ESI†), respectively. There is no noticeable difference in the NIH3T3 cells treated with ZGC@PAA and ZGC@PEG@PAA-RGD, due to the absence of integrin on the surfaces of healthy cells.

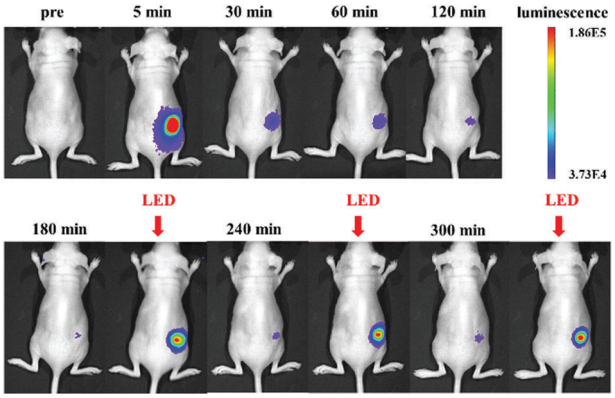

Fig. 6 *In vivo* NIR luminescent images of a normal mouse after subcutaneous injection with ZGC@PEG@PAA nanocrystals (3.6 mg mL^{-1}, 50 μL) which were pre-excited with 254 nm UV light for 10 min before injection. The mouse was irradiated with 657 nm LED light for 3 min at 3 h post injection, and then re-irradiated at intervals of 1 h after that.

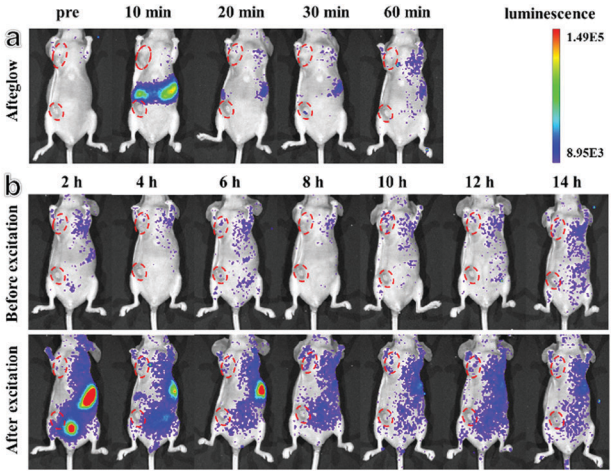

Fig. 7 *In vivo* luminescent images of 4T1 tumor-bearing mice after oral administration of (a) ZGC@PEG@PAA-RGD NCs (3.6 mg mL^{-1}, 200 μL, excited with 254 nm UV light for 10 min before injection); (b) the mouse NCs were irradiated with a LED lamp (657 nm) for 3 min at different times after oral administration. The exposure time for collecting images was 60 s. The parallel experiments were set as n = 3.

All the *in vitro* results indicate that the RGD-modified highly fluorescent ZGC nanocrystals could be efficiently taken up by the cancer cells and used for *in vivo* long term targeted imaging of cancer. To test the feasibility of *in vivo* imaging, 50 μL of ZGC@PEG@PAA nanocrystals (3.6 mg mL^{-1}) were excited for 10 min using a 254 nm UV lamp, and then subcutaneously injected into a healthy nude mouse. The luminescence was collected *via* an IVIS Lumina XRMS Series III Imaging System. The images in Fig. 6 clearly demonstrate that the afterglow of ZGC nanocrystals can last for about 3 h without any re-excitation, and there was no autofluorescence from the nude mouse. After the luminescence had decayed, 657 nm light from a LED lamp was used to re-excite the nanocrystals for 3 min, and strong luminescence was observed again. More importantly, these injected nanocrystals can be repeatedly excited many times, showing the great potential for long-term *in vivo* imaging.

In contrast to most RGD-modified nanoparticles which are intravenously injected for targeted imaging or therapy, the *in vivo* tumor targeting and imaging in this case was performed by oral administration of the RGD-modified ZGC nanocrystals. The oral administration route was selected because it has minimal side effects (noninvasive in nature) due to the protection afforded by the digestive tract during diagnosis and treatment,[59] and easy acceptance, as well as its convenience.[39,60] The un-modified nanocrystals (*i.e.*, ZGC@PEG@PAA) were used to compare with the RGD-modified probes. The same amounts of both the modified and un-modified ZGC nanocrystals (3.6 mg mL^{-1}, 200 μL) were pre-excited with 254 nm UV light for 10 min, and then respectively delivered into 4T1-bearing tumor mice by gavage administration. Each mouse had two tumors at the second and fourth breast on the right side, respectively. The *in vivo* afterglow luminescence and images were collected using the same imaging instrument (*i.e.*, an IVIS Lumina XRMS Series III Imaging System). In the first 10 min, the bright luminescence of the nanocrystals was mainly detected in the stomach and the intestine (Fig. 7a and Fig. S10a, ESI†). The luminescence can last for about 2 h without excitation, and weak luminescence at the tumor site was observed during the first 2 h. Then, the mice were irradiated with 657 nm light for 3 min at intervals of 2 h (Fig. 7b). Strong luminescence at the tumor site was observed at 4 h post-administration, reached its maximum at 8 h, and then decreased due to the dynamic accumulation of nanocrystals. In the control group, the luminescence at the tumor site was much weaker in the same time frame (Fig. S10b, ESI†), due to the lesser accumulation of nanocrystals arising from the absence of a RGD peptide. This result demonstrates the excellence of RGD peptides for targeted imaging. Interestingly, the upper tumor near the "armpit" of the front left leg exhibits stronger luminescence than the one at the abdomen, which could be due to the rich lymph nodes and the metastasis of tumor cells near the "armpit."[61]

It is known that RGD peptides can be degraded under the harsh conditions in the stomach. Fig. S11 (ESI†) shows the variation of UV-vis absorbance of RGD functionalized ZGC nanocrystals in the presence of pepsin under strong acidic conditions (pH = 1–2), which are similar to that of stomach conditions. The results show the partial decomposition of the RGD peptide under these harsh conditions. Our results demonstrate that RGD-modified ZGC nanocrystals could be orally delivered and used for targeted imaging of the tumor, although they lose some targeting capacity due to the harsh conditions in the stomach.

To evaluate the biodistribution of ZGC nanocrystals in tumor-bearing mice, the major organs (*i.e.*, heart, liver, spleen, lung, kidney, tumor stomach, and intestines) were excised at 8 h after oral administration of the RGD-modified and un-modified nanocrystals (*i.e.*, ZGC@PEG@PAA-RGD and ZGC@PEG@PAA nanocrystals). As shown in Fig. 8, both the modified and un-modified ZGC nanocrystals mainly remain in the stomach, lung, and intestines, as indicated by their stronger afterglow

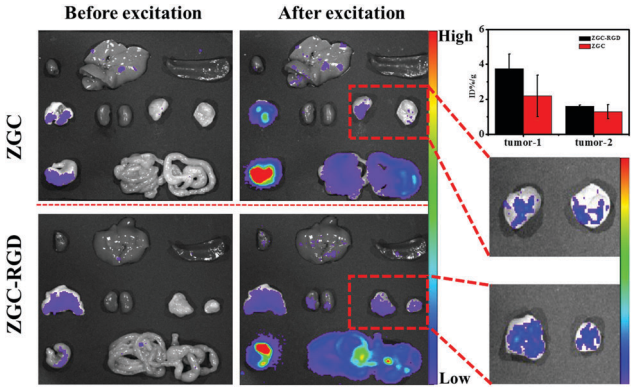

Fig. 8 *Ex vivo* luminescence images of the heart, liver, spleen, lung, kidney, tumor-1, tumor-2, stomach, and intestines from the 4T1 tumor-bearing mouse collected at 8 h post oral administration of ZGC@PEG@PAA (top) and ZGC@PEG@PAA-RGD (bottom). Tumor-1 and tumor-2 refer to the tumors in the second and fourth breast on the right side of the mouse, respectively.

luminescence in comparison with other organs. More unmodified ZGC nanocrystals are accumulated in the stomach than RGD-modified nanocrystals. The ZGC@PEG@PAA-RGD nanocrystals are uniformly distributed in the lung in comparison with the unmodified ZGC nanocrystals. These organs exhibit afterglow luminescence after they were excited by 657 nm light from a LED lamp for 3 min. The luminescence in the tumors from the mouse orally administrated with the RGD-modified nanocrystals is stronger than that in the mice treated with the unmodified nanocrystals. In both cases, the tumor in the second breast in the right side of the mouse (referred as tumor-1) shows a brighter persistent luminescence than the tumour in the fourth breast on the right side (referred to as tumor-2) due to its higher content than tumor 2 (*i.e.*, 3.9%ID g^{-1} *vs.* 1.9%ID g^{-1} in the case of oral administration of RGD-modified ZGC). In contrast, the persistent luminescence in the heart, liver, spleen, and kidney is much weaker, and the luminescence in the kidney from the mouse administrated with RGD-modified nanocrystals is stronger than that treated with unmodified nanocrystals. These results are consistent with the *in vivo* imaging in Fig. 7 and Fig. S10 (ESI†), illustrating that modification of ZGC nanocrystals with a RGD-peptide improved the blood circulation, biodistribution and targeting ability of the nanocrystals.

To further demonstrate the dynamic accumulation of ZGC nanocrystals in the tumor, highly sensitive SPECT/CT imaging was performed after the RGD-modified and unmodified nanocrystals were labeled with the clinically used radioisotope ^{99m}Tc (half-life, $t_{1/2}$ = 6.02 h, gamma-ray emission energy: 140 keV).[62–64] It should be noted that both nanocrystals have a similar hydrodynamic size before and after labeling with ^{99m}Tc (Fig. 9a). The labeled nanocrystals (3.6 mg mL^{-1}, 100 μL) were orally delivered into the stomach. Obviously, there is a relatively remarkable emission of gamma rays from the ^{99m}Tc-ZGC@PEG@PAA-RGD accumulated in the tumor after oral administration (Fig. 9b). In addition, strong signals were found from the stomach, intestine, and bladder. In contrast, only weak gamma ray emissions at the tumor sites from the

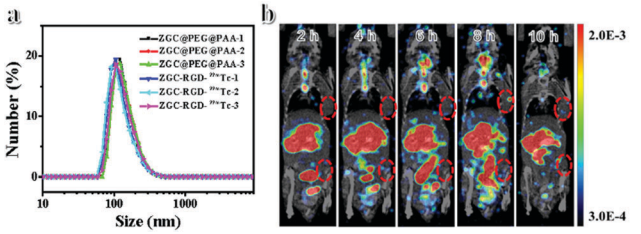

Fig. 9 (a) Hydrodynamic size of the ZGC@PEG@PAA nanocrystals and ^{99m}Tc-labeled ZGC nanocrystal solutions; (b) *in vivo* SPECT/CT images of the 4T1 tumor-bearing mice after oral administration of ^{99m}Tc-labeled ZGC@PEG@PAA-RGD NCs. The tumors are indicated by the red circles.

accumulated ^{99m}Tc labeled ZGC@PEG@PAA were observed (Fig. S12, ESI†). These results are consistent with those from luminescence imaging.

The intense luminescence in the intestinal tract and bladder imply that ZGC nanocrystals might be cleared out through renal excretion and intestinal metabolism. The luminescence of ZGC nanoparticles in feces and urine were measured, and the obvious

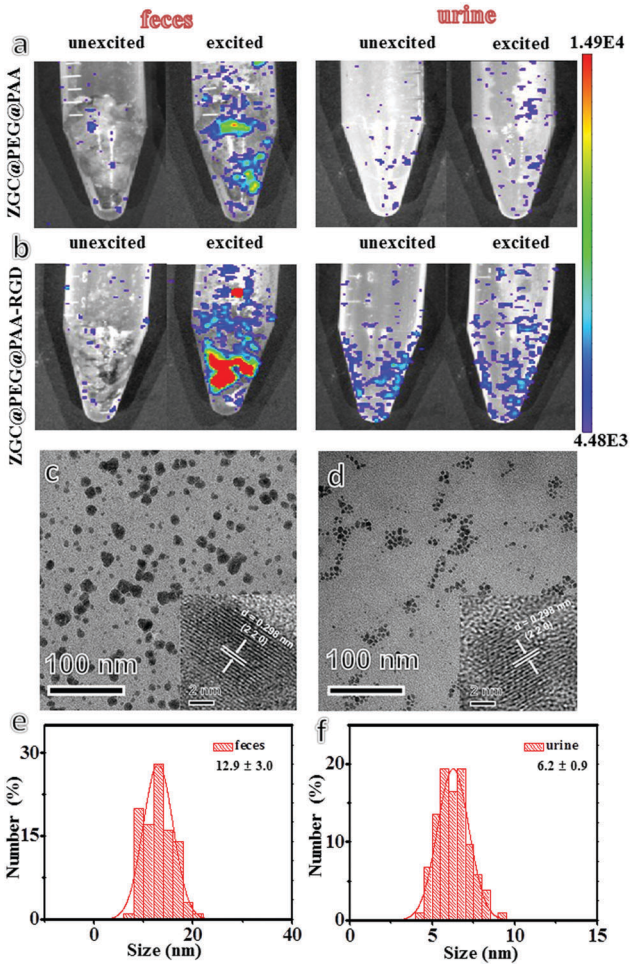

Fig. 10 (a and b) Luminescent images of feces and urine collected from mice respectively administered with ZGC@PEG@PAA and ZGC@PEG@PAA-RGD NCs; (c and d) TEM images with HRTEM images in the insets and (e and f) size distributions of ZGC particles found in feces (c, e) and urine (d, f).

difference in the luminescence intensity before and after excitation by a LED lamp [Fig. 10(a and b)] demonstrates that modification of ZGC nanoparticles with RGD peptides could improve their clearance. To demonstrate the morphology and composition of nanoparticles found in feces and urine, the feces and urine of mice were purified to collect the nanoparticles, which were characterized using TEM [Fig. 10(c and d)]. The nanoparticles found in urine have a smaller size [(6.2 ± 0.9) nm] and a narrower size distribution than those found in feces [(12.9 ± 3.0) nm]. Their HRTEM images clearly present lattice fringes with an interplanar spacing of 0.298 nm which matches well with the (220) plane of spinel $ZnGa_2O_4$ and demonstrate the *in vivo* stability of the nanocrystals. The clearance of ZGC nanocrystals through feces and urine could minimize their potential side effects.

Conclusion

In summary, highly bright, long afterglow ZGC nanocrystals were successfully prepared using a one-step hydrothermal method. The resultant ZGC nanocrystals exhibit an absolute fluorescence quantum yield of 20% and 5 days of afterglow. Their luminescence can be activated repetitively by 657 nm LED light for deep tissue penetration and long-term bioimaging. They were functionalized with a c(RGDyK) peptide and the radioisotope ^{99m}Tc for successful targeted imaging of orthotopic breast cancer through afterglow luminescence imaging and SPECT/CT imaging after oral administration. The stronger signal at the tumor sites when using both imaging methods demonstrates the great potential of multifunctional persistent luminescent probes in the targeted imaging of cancer cells.

Methods and experimental

Materials

Zinc nitrate hexahydrate [$Zn(NO_3)_2{\cdot}6H_2O$, 98%], gallium nitrate hydrate [$Ga(NO_3)_3{\cdot}xH_2O$, 99.9%], chromium nitrate nonahydrate [$Cr(NO_3)_3{\cdot}9H_2O$, 99%], ammonium hydroxide (28%, wt), hydrochloride acid (analytical grade), isopropyl alcohol and sodium hydroxide were used as received. α,ω-Dicarboxyl-terminated PEG (HOOC–PEG–COOH, M_W = 2000) was prepared as described elsewhere.[65] Polyacrylic acid (PAA, average M_W = 3000) was purchased from Aladdin (Shanghai, China). Phosphate buffer solution (PBS, pH = 7.4) was purchased from Shanghai Hongbei Reagent Co. *N*-Hydroxysuccinimide (NHS) was purchased from J&K and *N*-(3-dimethylaminopropyl)-*N*′-ethylcarbodiimide hydrochloride (EDC) was purchased from Aladdin. c(RGDyK) peptide (M_W = 722.38) was obtained from Bankpeptide Co. Ltd (Hefei, China). Milli-Q water (Millipore, USA, resistivity >18 MΩ cm) was used in the experiments.

Synthesis of size tunable Cr^{3+} doped $ZnGa_2O_4$ nanocrystals

The Cr^{3+} doped $ZnGa_2O_4$ nanoparticles were prepared using a hydrothermal method. Typically, 3.6 mmol $Zn(NO_3)_3{\cdot}6H_2O$, 6 mmol $Ga(NO_3)_3{\cdot}xH_2O$, and 0.012 mmol $Cr(NO_3)_3{\cdot}9H_2O$ were dissolved in 15 mL of Milli Q water. Around 3 mL of ammonium hydroxide (28%, wt) was quickly added into the above mixture to adjust its pH to 9–9.5. The transparent solution rapidly became turbid, and the formed suspension was stirred vigorously for 30 min. The suspension was then transferred into a Teflon-lined autoclave (25 mL) and hydrothermally treated at 220 °C for 10 h. After natural cooling to room temperature, the thus-formed white precipitates were separated through centrifugation, and washed with 0.01 M HCl several times to remove ZnO impurities. The purified ZGC nanocrystals were redispersed in Milli-Q water for further characterization, and surface modification. The particle size can be tuned by changing the reaction parameters and Table 1 shows the parameters used to prepare 8.7, 14.2, 20.6, and 32.4 nm ZGC nanocrystals.

Functionalization of ZGC nanocrystals

The above purified ZGC nanoparticles were used for surface modification. Specifically, 20 mg ZGC nanoparticles were dispersed in 20 mL of 0.9 mM HCl solution, and vigorously stirred for 30 min. Then, 743.9 mg HOOC–PEG–COOH was added into the solution and stirred overnight to form a clear and relatively transparent solution. The resultant nanoparticles (denoted as ZGC@PEG) were purified by ultrafiltration and diluted to 20 mL with Milli-Q water. To further modify the ZGC@PEG nanoparticles with PAA, 0.1 M NaOH was used to adjust the pH of the diluted solution to 8–10, and then 892.7 mg PAA was added into the solution and stirred overnight. The modified nanoparticles (denoted as ZGC@PEG@PAA) were purified by ultrafiltration at 4500 rpm several times by using a membrane with a molecular weight cutoff of 100 kDa.

To conjugate the modified nanoparticles with RGD peptide for tumor-targeted imaging, 100 μL (3.6 mg mL^{-1}) of ZGC@PEG@PAA solution was added into 10 mL PBS (pH = 6.5) solution, and then 1-ethyl-3-(3-dimethylaminopropyl) carbodiimide hydrochloride (EDC·HCl, 4 mg) and *N*-hydroxysuccinimide (NHS, 10 mg) were added into the mixture sequentially. The above mixture was stirred for 2 h. Next, 18 mg c(RGDyK) was added into the solution and the pH of the above mixed solution was adjusted to 8 using 0.1 M NaOH. The unreacted RGD was removed by centrifugation through a High Speed Refrigerated Centrifuge (Beckman Allegra 64R, USA), and the conjugates (denoted as ZGC@PEG@PAA-RGD) were washed (20 000 rpm, 15 min) several times with PBS (pH = 6.5) solution and finally dispersed in 0.9% NaCl solution.

Characterization of ZGC nanoparticles

The morphology and crystal structure of the ZGC nanocrystals were characterized through an FEI Tecnai G2 field emission high-resolution transmission electron microscope (HRTEM) with an accelerating voltage of 200 kV. The ZGC nanopowder obtained by natural drying was characterized using a Shimadzu XRD-6000 X-ray diffractometer equipped with Cu Kα1 radiation (λ = 0.15406 nm). The scanning rate was 0.05 s^{-1} for collecting the diffraction data in the range $20^\circ < 2\theta < 80^\circ$. The hydrodynamic size and zeta potential of the ZGC colloids were measured at 25 °C using a dynamic light scattering instrument

(Zetasizer Nano ZS90, Malvern). The absorption spectra were recorded on a UV-3600 ultraviolet-visible-near-infrared (UV-vis-NIR) spectrophotometer (Shimadzu, Kyoto, Japan). Fourier transform infrared (FTIR) spectra (4000–500 cm^{-1}) were collected on a Magna-560 spectrometer (Nicolet, Madison, USA). The fluorescence spectra and afterglow decay curves were collected on a FLS980 spectrometer (Edinburgh Instruments, UK). The concentration of ZGC nanocrystals was quantified using inductively coupled plasma-mass spectroscopy (ICP-MS) (Thermo Elemental, UK). The absorbance of the formazan formed during the MTT assay was measured by a microplate reader (Thermo, Varioskan Flash). The *in vivo* imaging of the mouse was performed using a IVIS Lumina XRMS Series III Imaging System (PerkinElmer, America) with a XGI-8 system. The single-photon emission computed tomography – computed tomography (SPECT/CT) imaging was performed on an animal SPECT (MILabs, Utrecht, the Netherlands) imaging system.

Measurement of absolute photoluminescence quantum yield

The excitation and emission spectra of the ZGC nanocrystals, as well as their absolute photoluminescence quantum yield (QY), were measured using an Edinburgh Instruments FLS980 spectrometer equipped with an integrating sphere. In detail, a quartz cuvette containing 3 mL of sample solution was used and 3 mL of Milli-Q water was set as a reference. The fluorescence emission spectra were collected in the range of 500–800 nm and excitation spectra in the range of 250–285 nm. The QY of the ZGC nanocrystals can be expressed by eqn (1),[66,67]

$$\begin{aligned} \mathrm{QY} &= \frac{\text{number of photons emitted}}{\text{number of photons absorbed}} \\ &= \frac{\int L(\text{sample})}{\int E(\text{reference}) - \int E(\text{sample})} \end{aligned} \quad (1)$$

where L(sample) is the photoluminescence intensity of the ZGC aqueous solution (1 mg mL^{-1}), E(reference) and E(sample) are the excitation light intensities of the reference and the sample, respectively.[68] $\int L(\text{sample})$ is the area under the curve of the photoluminescence spectrum of the ZGC sample, and $\int E(\text{reference}), \int E(\text{sample})$ are the areas under the excitation spectra of the reference and the sample,[23] respectively.

Cytotoxicity assay and cell imaging

4T1 murine breast cancer cells were cultured in 96-well plates with a standard cell medium at 37 °C in a 5% CO_2 atmosphere for 24 h, and the density of the 4T1 cells was about 8000 per well. The original medium was removed and the cells were washed with 100 μL PBS and then incubated with the ZGC@PEG@PAA and ZGC@PEG@PAA-RGD nanocrystals which were diluted with the culture medium to different concentrations (*i.e.*, 0, 5, 10, 20, 40, 80, 160 μg mL^{-1}) for another 24 h, respectively. After that, the cells were washed with another 100 μL PBS and incubated with 100 μL medium containing 10% 5 mg mL^{-1} MTT for 4 h. After the removal of the culture medium, 100 μL dimethyl sulfoxide (DMSO) was added into each well to dissolve the thus-formed formazan crystals. The absorption of formazan solution was measured at 490 nm on a microplate reader (Thermo, Varioskan Flash). The cell viability was calculated using eqn (2).

$$\text{Cell viability (\%)} = A_T/A_C \times 100\% \quad (2)$$

where A_T is the mean absorbance of the treatment group, and A_C is the mean absorbance of the control.

For cell imaging, 4×10^4 T1 murine breast cancer cells were seeded into 35 mm glass bottom culture dishes incubated with 4T1 cells at 37 °C for 24 h. The culture medium was removed, and fresh RPMI medium containing 0.1 mg as-prepared ZGC@PEG@PAA and ZGC@PEG@PAA-RGD nanocrystals was added into the culture dishes, respectively. After culturing for another 24 h, the medium was discarded and the cells were washed with PBS solution (pH = 7.2–7.4) twice. Afterward, the cells were fixed with 70% ice ethyl alcohol for 30 min, and washed several times with PBS. Then, Hoechst dye (1 mL, 10 μg mL^{-1}) was used to stain the nuclei of the cells for 5 min in a dark room, followed by washing with PBS several times. As a control, U87 cells and NIH3T3 cells were treated using the same procedure. The cell uptake of nanocrystals was observed using confocal fluorescence microscopy.

To further evaluate the difference in endocytosis of 4T1 cells toward the ZGC@PEG@PAA and ZGC@PEG@PAA-RGD nanocrystals *in vitro*, 2.5×10^5 4T1 cells were cultured in RPMI (1640) medium with these ZGC nanocrystals in 60 × 15 mm culture dishes for 24 h. Then, the cells were washed several times with PBS, digested by trypsinization, and collected *via* centrifugation. The afterglow signal of the cells was obtained using a CCD camera of a IVIS Lumina XRMS Series III Imaging System (PerkinElmer, America) with a XGI-8 gas anesthesia system, after excitation with a 254 nm UV lamp for 10 min or a LED lamp for 3 min. The exposure time during signal collection was set to be 60 s. The intensity and wavelength of the LED lamp were 30 W and 657 nm, respectively.

Animal model

Specific pathogen free (SPF) grade nude female mice (15–20 g) were purchased from Shanghai SLAC Laboratory Animal Co., Ltd and used under protocols approved by the Laboratory Animal Center of Soochow University. The tumors were grafted by subcutaneous inoculation of 2×10^6 4T1 cells in about 50 μL PBS into the breast of each mouse. The tumor gradually grew to around 100 mm^3 within 10 days, and the mice could then be used for imaging experiments. The nude mice were fasted for 24 h before oral administration of ZGC nanoprobes.

In vivo imaging

ZGC@PEG@PAA and ZGC@PEG@PAA-RGD nanoparticles were respectively dispersed in 0.9% NaCl solution (3.6 mg mL^{-1}) and excited with a 254 nm UV lamp for 10 min. Then 200 μL of the two types of as prepared nanoparticles were delivered into different 4T1 tumor-bearing nude mice through intra-gastric administration, respectively. After the luminescence of the ZGC nanocrystals had decayed until it could not be detected with the IVIS Lumina II imaging system, the same LED lamp was

adopted to irradiate the mice for 3 min, and the luminescent signals were collected again using the same instrument.

^{99m}Tc labeled ZGC NPs for SPECT imaging

Na[$^{99m}TcO_4$] was purchased from Shanghai GMS Pharmaceutical Co., Ltd 20 μL $SnCl_2$ (1 mg mL^{-1}, in 0.01 M HCl) solution was added into 300 μL Na[$^{99m}TcO_4$] solution with a radioactivity of about 3 mCi and then vibrated gently for 5 min. The ZGC@PEG@PAA or ZGC@PEG@PAA-RGD NP solution (200 μL, 3.6 mg mL^{-1}) was added into the above radioactive solution and vibrated gently for 30 min at room temperature. The obtained ^{99m}Tc labeled ZGC (denoted as ^{99m}Tc-ZGC or ^{99m}Tc-ZGC-RGD for short) nanoparticle solutions were purified *via* ultrafiltration to remove free ^{99m}Tc and concentrated to about 200 μL. The radiolabeling yields were estimated to be around 54% (^{99m}Tc-ZGC) and 78% (^{99m}Tc-ZGC-RGD), respectively. 100 μL ^{99m}Tc-ZGC or ^{99m}Tc-ZGC-RGD nanoparticles were delivered into the stomachs of 4T1 tumor-bearing mice through gavage and the SPECT/CT images were collected by using an animal SPECT/CT (MILabs, Utrecht, the Netherlands) imaging system after various times.

The extraction of nanoparticles from feces and urine

The feces and urine of the tumor-bearing nude mice that were orally administered with ZGC@PEG@PAA or ZGE@PEG@PAA-RGD nanoparticles were continuously collected using a metabolic cage. The feces were dispersed in Milli Q water by ultrasonic processing, and then separated at 6000 rpm for 10 min. The supernatant was dialyzed against Milli Q water with a universal dialysis tube [molecular weight cut-off (MWCO) of 8–14 kDa] for 48 h to remove impurities. The dialysis solution was lyophilized for further use.

Conflicts of interest

There are no conflicts to declare.

Acknowledgements

Z. Li acknowledges support from the National Natural Science Foundation of China (81471657, 81527901), the 1000 Plan for Young Talents, Jiangsu Specially Appointed Professorship, and Jiangsu Provincial program for innovative and entrepreneurial talents. The authors are also grateful for support from the Jiangsu Provincial Key Laboratory of Radiation Medicine and Protection, the Priority Academic Development Program of Jiangsu Higher Education Institutions (PAPD). The authors would like to thank Dr Tania Silver for helpful discussions regarding the manuscript.

References

1 A. Signore, S. J. Mather, G. Piaggio, G. Malviya and R. A. Dierckx, *Chem. Rev.*, 2010, **110**, 3112–3145.
2 N. Deshpande, A. Needles and J. K. Willmann, *Clin. Radiol.*, 2010, **65**, 567–581.
3 M. Mehrmohammadi, T.-H. Shin, M. Qu, P. Kruizinga, R. L. Truby, J.-H. Lee, J. Cheon and S. Y. Emelianov, *Nanoscale*, 2013, **5**, 11179–11186.
4 A. Abdukayum, C.-X. Yang, Q. Zhao, J.-T. Chen, L.-X. Dong and X.-P. Yan, *Anal. Chem.*, 2014, **86**, 4096–4101.
5 A. Srivatsan, X. Chen, M. G. Pomper and P. B. Fisher, *Adv. Cancer Res.*, Academic Press, 2014, vol. 124, pp. 83–129.
6 A. Hellebust and R. Richards-Kortum, *Nanomedicine*, 2012, **7**, 429–445.
7 Z. Li, Q. Sun, Y. Zhu, B. Tan, Z. P. Xu and S. X. Dou, *J. Mater. Chem. B*, 2014, **2**, 2793–2818.
8 D. L. Daugherty and S. H. Gellman, *J. Am. Chem. Soc.*, 1999, **121**, 4325–4333.
9 M. Montalti, L. Prodi, E. Rampazzo and N. Zaccheroni, *Chem. Soc. Rev.*, 2014, **43**, 4243–4268.
10 S. Bhaumik, X. Z. Lewis and S. S. Gambhir, *J. Biomed. Opt.*, 2004, **9**, 578–586.
11 Y. Zhu, H. Hong, Z. P. Xu, Z. Li and W. Cai, *Curr. Mol. Med.*, 2013, **13**, 1549–1567.
12 Y. Zhu, Z. Li, M. Chen, H. M. Cooper, G. Q. Lu and Z. P. Xu, *Chem. Mater.*, 2012, **24**, 421–423.
13 Y. Zhu, Z. Li, M. Chen, H. M. Cooper, G. Q. M. Lu and Z. P. Xu, *J. Colloid Interface Sci.*, 2013, **390**, 3–10.
14 H. Zhang, X. Huang, L. Li, G. Zhang, I. Hussain, Z. Li and B. Tan, *Chem. Commun.*, 2012, **48**, 567–569.
15 X. Huang, Y. Luo, Z. Li, B. Li, H. Zhang, L. Li, I. Majeed, P. Zou and B. Tan, *J. Phys. Chem. C*, 2011, **115**, 16753–16763.
16 C. Liu, Z. Gao, J. Zeng, Y. Hou, F. Fang, Y. Li, R. Qiao, L. Shen, H. Lei, W. Yang and M. Gao, *ACS Nano*, 2013, **7**, 7227–7240.
17 M. Jiao, L. Jing, C. Liu, Y. Hou, J. Huang, X. Wei and M. Gao, *Chem. Commun.*, 2016, **52**, 5872–5875.
18 Y. Hou, R. Qiao, F. Fang, X. Wang, C. Dong, K. Liu, C. Liu, Z. Liu, H. Lei, F. Wang and M. Gao, *ACS Nano*, 2013, **7**, 330–338.
19 T. Maldiney, G. Byk, N. Wattier, J. Seguin, R. Khandadash, M. Bessodes, C. Richard and D. Scherman, *Int. J. Pharm.*, 2012, **423**, 102–107.
20 T. Maldiney, M. U. Kaikkonen, J. Seguin, Q. le Masne de Chermont, M. Bessodes, K. J. Airenne, S. Ylä-Herttuala, D. Scherman and C. Richard, *Bioconjugate Chem.*, 2012, **23**, 472–478.
21 T. Maldiney, A. Bessière, J. Seguin, E. Teston, S. K. Sharma, B. Viana, A. J. J. Bos, P. Dorenbos, M. Bessodes, D. Gourier, D. Scherman and C. Richard, *Nat. Mater.*, 2014, **13**, 418–426.
22 T. Matsuzawa, Y. Aoki, N. Takeuchi and Y. Murayama, *J. Electrochem. Soc.*, 1996, **143**, 2670–2673.
23 B. B. Srivastava, A. Kuang and Y. Mao, *Chem. Commun.*, 2015, **51**, 7372–7375.
24 A. Bessière, S. K. Sharma, N. Basavaraju, K. R. Priolkar, L. Binet, B. Viana, A. J. J. Bos, T. Maldiney, C. Richard, D. Scherman and D. Gourier, *Chem. Mater.*, 2014, **26**, 1365–1373.
25 Q. le Masne de Chermont, C. Chanéac, J. Seguin, F. Pellé, S. Maîtrejean, J.-P. Jolivet, D. Gourier, M. Bessodes and

D. Scherman, *Proc. Natl. Acad. Sci. U. S. A.*, 2007, **104**, 9266–9271.
26 T. Lécuyer, E. Teston, G. Ramirez-Garcia, T. Maldiney, B. Viana, J. Seguin, N. Mignet, D. Scherman and C. Richard, *Theranostics*, 2016, **6**, 2488–2524.
27 A. Bessière, S. Jacquart, K. Priolkar, A. Lecointre, B. Viana and D. Gourier, *Opt. Express*, 2011, **19**, 10131–10137.
28 Y.-J. Chuang, Z. Zhen, F. Zhang, F. Liu, J. P. Mishra, W. Tang, H. Chen, X. Huang, L. Wang, X. Chen, J. Xie and Z. Pan, *Theranostics*, 2014, **4**, 1112–1122.
29 A. Abdukayum, J.-T. Chen, Q. Zhao and X.-P. Yan, *J. Am. Chem. Soc.*, 2013, **135**, 14125–14133.
30 J. Wang, Q. Ma, Y. Wang, H. Shen and Q. Yuan, *Nanoscale*, 2017, **9**, 6204–6218.
31 T. Maldiney, C. Richard, J. Seguin, N. Wattier, M. Bessodes and D. Scherman, *ACS Nano*, 2011, **5**, 854–862.
32 E. Teston, S. Richard, T. Maldiney, N. Lièvre, G. Y. Wang, L. Motte, C. Richard and Y. Lalatonne, *Chem. – Eur. J.*, 2015, **21**, 7350–7354.
33 T. Maldiney, A. Lecointre, B. Viana, A. Bessière, M. Bessodes, D. Gourier, C. Richard and D. Scherman, *J. Am. Chem. Soc.*, 2011, **133**, 11810–11815.
34 Z. Pan, Y.-Y. Lu and F. Liu, *Nat. Mater.*, 2012, **11**, 58–63.
35 Y. Li, S. Zhou, Y. Li, K. Sharafudeen, Z. Ma, G. Dong, M. Peng and J. Qiu, *J. Mater. Chem. C*, 2014, **2**, 2657–2663.
36 M. Allix, S. Chenu, E. Véron, T. Poumeyrol, E. A. Kouadri-Boudjelthia, S. Alahraché, F. Porcher, D. Massiot and F. Fayon, *Chem. Mater.*, 2013, **25**, 1600–1606.
37 G. Ramírez-García, S. Gutiérrez-Granados, M. A. Gallegos-Corona, L. Palma-Tirado, F. d'Orlyé, A. Varenne, N. Mignet, C. Richard and M. Martínez-Alfaro, *Int. J. Adv. Pharm.*, 2017, **532**, 686–695.
38 Z. Li, Y. Zhang, X. Wu, L. Huang, D. Li, W. Fan and G. Han, *J. Am. Chem. Soc.*, 2015, **137**, 5304–5307.
39 Y.-J. Li and X.-P. Yan, *Nanoscale*, 2016, **8**, 14965–14970.
40 J. Shi, X. Sun, J. Zhu, J. Li and H. Zhang, *Nanoscale*, 2016, **8**, 9798–9804.
41 J. Wang, Q. Ma, X.-X. Hu, H. Liu, W. Zheng, X. Chen, Q. Yuan and W. Tan, *ACS Nano*, 2017, **11**, 8010–8017.
42 Y. Zhong, G. Tian, Z. Gu, Y. Yang, L. Gu, Y. Zhao, Y. Ma and J. Yao, *Adv. Mater.*, 2014, **26**, 2831–2837.
43 G. Ramírez-García, M. Martínez-Alfaro, F. d'Orlyé, F. Bedioui, N. Mignet, A. Varenne, S. Gutiérrez-Granados and C. Richard, *Int. J. Adv. Pharm.*, 2017, **532**, 696–703.
44 W. Fan, N. Lu, C. Xu, Y. Liu, J. Lin, S. Wang, Z. Shen, Z. Yang, J. Qu, T. Wang, S. Chen, P. Huang and X. Chen, *ACS Nano*, 2017, **11**, 5864–5872.
45 J. Shi, X. Sun, J. Li, H. Man, J. Shen, Y. Yu and H. Zhang, *Biomaterials*, 2015, **37**, 260–270.
46 T. Maldiney, B. Ballet, M. Bessodes, D. Scherman and C. Richard, *Nanoscale*, 2014, **6**, 13970–13976.
47 J. Shi, M. Sun, X. Sun and H. Zhang, *J. Mater. Chem. B*, 2016, **4**, 7845–7851.
48 H. M. Kim, H. Lee, K. S. Hong, M. Y. Cho, M.-H. Sung, H. Poo and Y. T. Lim, *ACS Nano*, 2011, **5**, 8230–8240.
49 T. Maldiney, B.-T. Doan, D. Alloyeau, M. Bessodes, D. Scherman and C. Richard, *Adv. Funct. Mater.*, 2015, **25**, 331–338.
50 E. Teston, Y. Lalatonne, D. Elgrabli, G. Autret, L. Motte, F. Gazeau, D. Scherman, O. Clément, C. Richard and T. Maldiney, *Small*, 2015, **11**, 2696–2704.
51 R. Zou, S. Gong, J. Shi, J. Jiao, K.-L. Wong, H. Zhang, J. Wang and Q. Su, *Chem. Mater.*, 2017, **29**, 3938–3946.
52 Y.-C. Lu, C.-X. Yang and X.-P. Yan, *Nanoscale*, 2015, **7**, 17929–17937.
53 S. Chenu, E. Veron, C. Genevois, A. Garcia, G. Matzen and M. Allix, *J. Mater. Chem. C*, 2014, **2**, 10002–10010.
54 P. Dhak, U. K. Gayen, S. Mishra, P. Pramanik and A. Roy, *J. Appl. Phys.*, 2009, **106**, 063721.
55 P. D. Rack, J. J. Peterson, M. D. Potter and W. Park, *J. Mater. Res.*, 2011, **16**, 1429–1433.
56 Y. Li, M. Gecevicius and J. Qiu, *Chem. Soc. Rev.*, 2016, **45**, 2090–2136.
57 M. Grinberg, *Opt. Mater.*, 2002, **19**, 37–45.
58 Y.-Y. Wang, L.-X. Lü, J.-C. Shi, H.-F. Wang, Z.-D. Xiao and N.-P. Huang, *Biomacromolecules*, 2011, **12**, 551–559.
59 A. des Rieux, V. Fievez, M. Garinot, Y.-J. Schneider and V. Préat, *J. Controlled Release*, 2006, **116**, 1–27.
60 J. D. Schulz, M. A. Gauthier and J.-C. Leroux, *Eur. J. Pharm. Biopharm.*, 2015, **97**(part B), 427–437.
61 W. Van den Broeck, A. Derore and P. Simoens, *J. Immunol. Methods*, 2006, **312**, 12–19.
62 S. Zhang, C. Sun, J. Zeng, Q. Sun, G. Wang, Y. Wang, Y. Wu, S. Dou, M. Gao and Z. Li, *Adv. Mater.*, 2016, **28**, 8927–8936.
63 X. Zhu, J. Li, Y. Hong, R. H. Kimura, X. Ma, H. Liu, C. Qin, X. Hu, T. Hayes, P. Benny, S. Sam Gambhir and Z. Cheng, *Mol. Pharmaceutics*, 2014, **11**, 1208–1217.
64 X. Jiang, S. Zhang, F. Ren, L. Chen, J. Zeng, M. Zhu, Z. Cheng, M. Gao and Z. Li, *ACS Nano*, 2017, **11**, 5633–5645.
65 Z. Li, L. Wei, M. Y. Gao and H. Lei, *Adv. Mater.*, 2005, **17**, 1001–1005.
66 J.-G. Kang, T.-J. Kim, C.-M. Park, L.-S. Woo and I.-T. Kim, *Chem. Soc.*, 2004, **25**, 704–710.
67 J.-C. Boyer and F. C. J. M. van Veggel, *Nanoscale*, 2010, **2**, 1417–1419.
68 J. C. de Mello, H. F. Wittmann and R. H. Friend, *Adv. Mater.*, 1997, **9**, 230–232.

